Observations on Floc Settling Velocities in the Tamar Estuary, United Kingdom

William H. McAnally, F.ASCE[1]; Ashish J. Mehta, M.ASCE[2]; and Andrew J. Manning[3]

Abstract: Measurements in the mesotidal Tamar estuary (UK) reported previously indicate a dependence of the floc settling velocity on the shear rate and the suspended fine sediment concentration or volume fraction. Typical time-independent analytic formulas for the floc settling velocity tend to follow the mean trend but fail to provide an explanation for the characteristic data spread. Moreover, they assume floc diameter to be single-valued such as the mean or the median. Given this constraint, an examination of tide-induced trends in the Tamar settling velocities is attempted by simple time-dependent modeling of aggregation, i.e., the dynamics of floc growth and breakup. The effect of aggregation on the settling velocity and diameter is simulated over a representative one-half tidal cycle. Starting at low water (LW) slack at the onset of the sediment erosional phase during the first quarter tide, as the shear rate and volume fraction increase, floc growth is shown to increase the settling velocity that peaks at a shear rate in the range of 15–30 s^{-1}. At higher shear rates, as floc breakup supersedes the effect of sediment concentration in promoting growth, the settling velocity gradually decreases until the shear rate reaches its maximum value on the order of 10^2 s^{-1} at the strength of flow. During the following depositional phase in the second quarter tide, as the shear rate decreases the settling velocity increases continually until high water (HW) slack when it achieves its overall maximum value as the shear rate approaches zero. Thus, the loci of settling velocity versus shear rate differ between the quarter tides and result in shear rate versus settling velocity hysteresis. Moreover, it is shown that in the Tamar, tidal variation prevents the settling velocity and diameter from always achieving the equilibrium assumed in analytic formulas. Thus, aggregation modeling serves as a useful guide for resolving temporal trends in floc properties.
DOI: 10.1061/(ASCE)WW.1943-5460.0000649.

Introduction

In the quantification of the rate of movement of flocculated sediment in estuaries, the settling velocity, arguably the most important transport property of flocs, is typically calculated from one of several time-independent analytic formulas, with many related to previous investigations such as those of Krone (1962), van Leussen (1994), Teeter (2001), and Winterwerp and van Kesteren (2004). These formulas are generally of the form

$$w_f = f(G, \phi) \tag{1}$$

where w_f = floc settling velocity; G = turbulent flow shear rate; $\phi = C/\rho_s$ = sediment volume fraction; C = concentration (dry mass per unit volume of suspension); and ρ_s = particle density. Formulas conforming to Eq. (1) are easy to use, and although they may lack some flexibility in tuning, their utility can be enhanced via additional physics-based relationships for some of the governing parameters (Strom and Keyvani 2011). On the other hand, such formulas do not account for the naturally occurring distribution of floc diameter d_f, and further assume that d_f and w_f are adequately represented by their equilibrium values. The main purpose of the present study was to explore the role of time-dependent aggregation of flocs, i.e., floc growth and breakup dynamics underpinning Eq. (1), in the tidal environment based on the multiclass representation of floc properties in terms of sediment mass. This is attempted for data from the Tamar estuary in the United Kingdom, and aggregation is simulated by basic time-dependent numerical modeling previously described in McAnally and Mehta (2000) and subsequently revised.

The article begins with a brief description of the estuarine site, transducers deployed, and method of measurement. Subsequent sections elaborate on the method of simulation, its application to the Tamar, and interpretation of the temporal effect of tide on the settling velocity. Lastly, the significance of simulation is briefly discussed relative to data trends including limitations of the experimental method and the modeling approach.

Measurements

Fig. 1 shows the study reach of the mesotidal Tamar near Calstock in Cornwall, about 30 km north of the estuary mouth near Plymouth. The reach is nominally 80 m wide with a mean depth of about 3 m and a semidiurnal tidal range varying from 2.2 m at neap to 4.7 m at spring, a mean range of about 3.5 m, and an annual mean river discharge of about 20 m^3 s^{-1}. The suspended fine sediment is largely made up of clay minerals dominated by kaolinite followed by illite and smectite. Measurements in a thin surficial layer of the intertidal bottom mud have indicated the presence of particulate organic carbon associated with Chlorophyll-a, the main source of extracellular polymeric substances (EPS), which characteristically mediate the structure of mineral flocs by biopolymeric adhesion and binding (Uncles et al. 2003).

The method to measure the settling velocity and related variables is described in detail in Manning (2001) and summarized in

[1]Engineer, Dynamic Solutions, LLC, Knoxville, TN 37919; Research Professor Emeritus, Geosystems Research Institute, Mississippi State Univ., Starkville, MS 39762 (corresponding author). Email: whmcanally@dsllc.com

[2]Principal, Nutech Consultants, Inc., 5605 Northwest 45th Lane, Gainesville, FL 32606. Email: mehtanutechinc@gmail.com

[3]Lecturer, Institute of Marine Studies, Plymouth Univ., Plymouth, UK; Principal Scientist, HR Wallingford, Wallingford, Oxfordshire OX10 8BA, UK. Email: andymanning@yahoo.com

Note. This manuscript was submitted on September 29, 2020; approved on March 25, 2021; published online on May 26, 2021. Discussion period open until October 26, 2021; separate discussions must be submitted for individual papers. This paper is part of the ***Journal of Waterway, Port, Coastal, and Ocean Engineering***, © ASCE, ISSN 0733-950X.

Manning and Dyer (2002a). In brief, the deployed instrument assembly POST (Profile Of Sediment Transport) consisted of a bottom-tethered metallic pole with miniaturized electromagnetic current meters (Christie et al. 1997) located 0.25 and 0.80 mab (m above bottom), optical backscatter transducers for suspended sediment concentration (Downing and Beach 1989) at 0.20, 0.60 and 1 mab, and a pressure gage for water depth. Vertical profiles of salinity and temperature were obtained with an SBE 19 SEACAT Profiler (Sea-Bird Electronics, Bellevue, WA). Altogether 10 deployments of the POST were made between August 4 and September 23, 1998, and one more on April 15, 2003. The duration of each ranged from 1 to 24 h, and, overall, the tidal range varied between neap and spring.

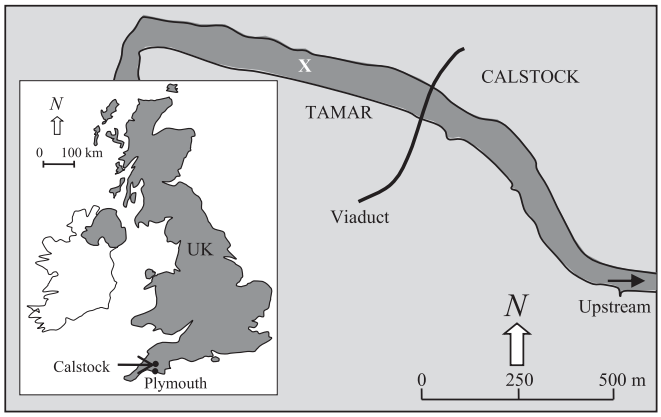

Fig. 1. Tamar estuary at Calstock in Cornwall, UK. X = location of POST.

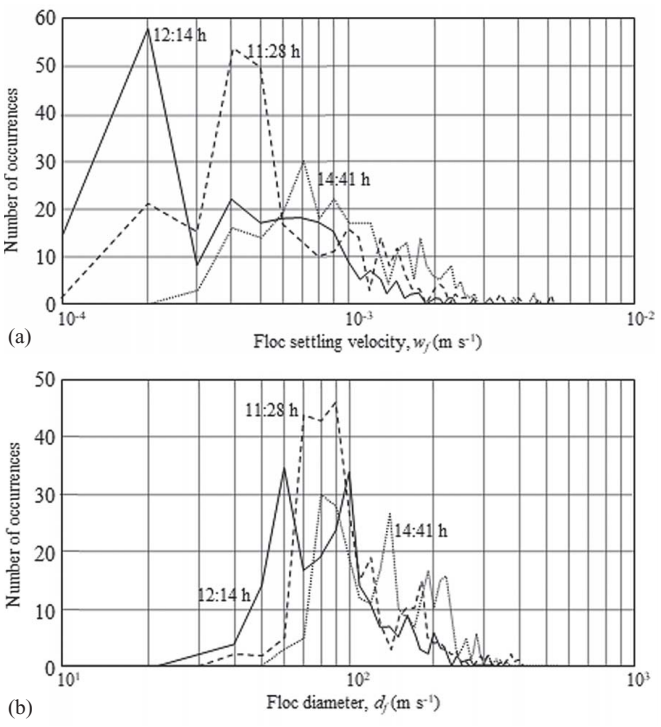

Fig. 2. (a) Tamar floc settling velocity distributions on August 5, 1998; and (b) Tamar floc diameter distributions on August 5, 1998.

Measurements to determine the settling velocity were made in situ using INSSEV (IN-Situ SEttling Velocity instrument) tethered to POST at 0.5 mab (Manning and Dyer 2002b). This device included a large metallic chamber with remotely controlled flap doors fore and aft. To operate the system, initially the flaps were opened to allow the flow to pass through, and at the desired instant were shut to collect about 3 liters of the suspension. Flap design and closure rate were meant to reduce eddy turbulence and resulting floc damage (Manning 2001). Below the chamber and connected to it by an opening with a horizontal sliding gate, was a 180 mm tall by 100- mm square Perspex column abetting a high-resolution Puffin (model UTC 341, Custom Camera Designs Ltd of Wells, Somerset, UK) video camera flush-mounted along a side of the column. The centerline of the camera lens was 105 mm below the sliding gate and 75 mm above the column base. Captured water sample in the chamber was permitted to stand for about 20 s to abate initial turbulence before the sliding gate was remotely opened to let the flocs fall into the column. All particles at the center of the column were imaged as they passed within 1 mm depth of field, 45 mm from the lens. Floc settling velocity and diameter were obtained directly from stored video images and converted to actual values by image calibration. For each sample, the settling velocity and the diameter were reported for flocs numbering as high as several hundred.

Representative hydraulic parameters for the Tamar deduced from ancillary measurements were: $\rho_s = 2{,}386$ kg m^{-3}, water density, $\rho_w = 1{,}015$ kg m^{-3}, water viscosity $\eta_w = 1.02 \times 10^{-3}$ Pa s, and Manning's bed resistance coefficient $n = 0.015$. The annual mean tidal prism P in the study reach is estimated to be 1.2×10^6 m^3. Given annual mean discharge $Q = 20$ m^3 s^{-1}, semidiurnal period $T = 12.42$ h, and nominal flow cross-sectional area $A = 240$ m^2 below midtide, the Simpson number $QT/2P$ amounts to about 0.1, which is subjectively consistent with the estuary's partially stratified state on an annual basis (Dyer et al. 2002). However, mixing tends to vary widely; during deployments, the salinity varied between almost nil and about 10 psu, and stratification ranged from almost wedge-like to fully mixed.

Data Presentation

Examples of the frequency distributions of the settling velocity $\varphi(w_f)$ and diameter $\varphi(d_f)$ are shown in Figs. 2(a and b). They correspond to three consecutive suspension samples taken on August 5 at 11:28 a.m., 12:14 p.m., and 12:46 p.m. during ebb flow. Shape-wise, these distributions are surrogates for other times and deployments that produced similar data (Manning 2001). In Table 1, changes in the relevant parameters including the sediment volume fraction ϕ, the mean settling velocity w_{fm}, its normalized standard deviation (standard deviation divided by mean) σ_{wn}, mean diameter d_{fm}, and its normalized standard deviation σ_{dn}, are mainly tied to changes in the shear rate G. The $\varphi(w_f)$ distributions show strong single peaks, with w_f values spread over a wide range

Table 1. Parameters of distributions of settling velocities and diameters in Figs. 2(a and b)

Time (h)	G (s^{-1})	ϕ	No. of particles	w_{fm} (m s^{-1})	σ_{wn} (m s^{-1})	d_{fm} (μm)	σ_{dn} (μm)	ρ_{fm} (kg m^{-3})
11:28	19.2	5.03×10^{-5}	292	8.37×10^{-4}	0.93	117	0.55	1,127
12:14	4.5	3.27×10^{-5}	230	5.76×10^{-4}	0.84	99	0.48	1,107
14:41	8.0	9.35×10^{-5}	280	1.18×10^{-3}	0.60	147	0.41	1,160

J. Waterway, Port, Coastal, Ocean Eng., 2021, 147(5): 04021015

manifested by σ_{wn} values of the same order of magnitude as the respective means. The $\varphi(d_f)$ distributions either have a dominant single-peak or a double-peak and at 14:41 there were additional identifiable peaks. In contrast to w_{fm}, the dominant d_{fm} peaks occur within a comparatively narrower range straddling 80 μm as a stable value suggesting well-formed, resilient flocs over the 3 h 13 min duration. The difference in the character of $\varphi(w_f)$ versus $\varphi(d_f)$ is accounted for by changes in the floc density ρ_f as an independent variable in the relationship between w_f and d_f. Thus, in the last column of Table 1, the mean floc density ρ_{fm} varies, even though in a minor way compared to the overall range mentioned later.

Following Manning and Dyer (2002a), who based their calculations on the Stokes law of settling particles in quiescent water, w_f, d_f, and the floc excess density $\Delta\rho_f = \rho_f - \rho_w$ are interrelated by

$$w_f = \frac{g\Delta\rho_f}{18\eta_w} d_f^2 \tag{2}$$

where g = acceleration due to gravity. Use of Eq. (2) is acceptable as the fall Reynolds number $\mathrm{Re}_f = \rho_w w_f d_f/\eta_w$ using overall mean values of $w_f = 1.19 \times 10^{-3}$ m s^{-1} and $d_f = 152$ μm, is 0.18, implying particle falling in the viscous range. To simplify data presentation, floc diameters were assumed to be fractally self-similar, a reasonable approximation when the sediment mainly consists of mineral matter (Kranenburg 1994). Thus, from mass balance $\Delta\rho_f$ is related to $\Delta\rho_s$ by

$$\Delta\rho_f = \Delta\rho_s \left(\frac{d_f}{d_s}\right)^{D-3} \tag{3}$$

where d_s = *base* particle diameter, and the fractal dimension D is given by

$$D = \frac{\log(\Delta\rho_f/\Delta\rho_s)}{\log(d_f/d_s)} + 3 \tag{4}$$

Eliminating $\Delta\rho_f$ between Eqs. (2) and (3) yields

$$w_f = \frac{g\Delta\rho_s}{18\eta_w d_s^{D-3}} d_f^{D-1} \tag{5}$$

Eqs. (3) and (5) were found to best represent the data trend for the 123 pairs of values of w_f and d_f (conveniently dropping the subscript m in both cases and assuming each pair denotes mean values for a water sample) with $d_s = 10.7$ μm, and $D = 2$ to be constant for the entire floc population. The material density $\rho_s = 2{,}386$ kg m^{-3} compared to the typically higher 2,600–2,700 kg m^{-3} for the extant clayey minerals was due to the presence of about 10% organic matter (density 1,030 kg m^{-3}) by weight. The d_s value is an order of magnitude larger than the clay diameter of about 1 μm and suggests that the base particles were essentially tightly packed agglomerates composed of mineral particles oriented and bound by electrochemical forces as well as EPS (Lick 2009). Moreover, the d_s value is consistent with the transition floc diameter of about 10 μm between cohesionless and cohesive particles deduced from size data on marine fine sediments with wide-ranging properties (McCave et al. 1995; Migniot 1968). The fractal dimension of 2 is common for marine flocs (Khelifa and Hill 2006), and its normalized standard deviation of 0.037 indicates a uniform floc structure.

In Fig. 3, the w_f values are plotted against d_f along with Eq. (5). The settling velocity increases linearly with diameter, implying that the typical trend of decreasing floc density ρ_f with increasing d_f, deduced from Eq. (5) is subsumed by the effect of increasing d_f on w_f (Lick 2009). Notwithstanding the evident data spread, with $D = 2$ the trendline pegged by $d_s = 10.7$ μm yields

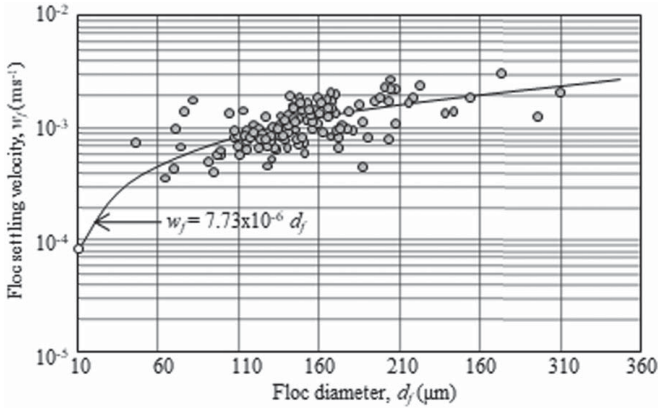

Fig. 3. Variation in Tamar floc settling velocity with diameter and best-fit equation.

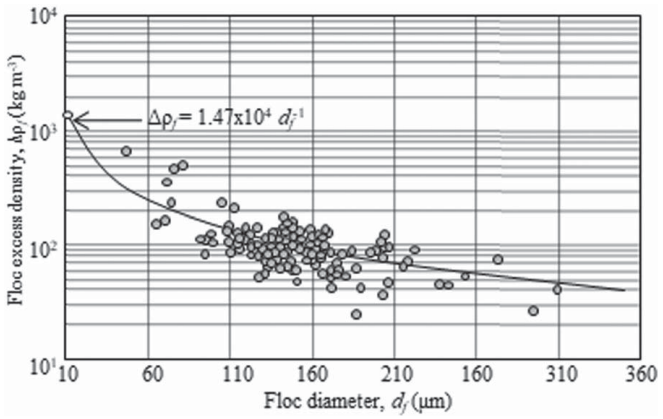

Fig. 4. Variation in Tamar floc excess density with diameter and best-fit equation.

$g\Delta\rho_s/18\eta_w d_s^{D-3} = 8 \times 10^{-6}$ s^{-1}. Referring to the corresponding relationship between $\Delta\rho_f$ and d_f in Fig. 4, in the absence of independent measurements of ρ_f, $\Delta\rho_f$ was obtained from Eq. (2) from w_f and d_f. Observe that $\Delta\rho_f$ rapidly declines with increasing d_f as the flocs become less densely packed and weaker. Eq. (3) can be rearranged as follows:

$$\Delta\rho_f = \frac{\Delta\rho_s d_s^{3-D}}{d_f^{3-D}} \tag{6}$$

where $\Delta\rho_s d_s^{3-D} = 1.467 \times 10^4$ kg m^{-2}; and $D = 2$ are best-fit values (constrained by the point 10.7, 2,386). As Eq. (3) was used to calculate ρ_f, the coefficients of the trendlines in Figs. 2 and 3 are interdependent.

The density of 119 flocs from the total 123 varied between 1,040 and 1,253 kg m^{-3} with an overall average of 1,113 kg m^{-3}, which is typical of estuarine flocs (Lick 2009), while the remaining four outliers ranged from 1,376 to 1,680 kg m^{-3}. For modeling purposes, given $d_s = 10.7$ μm, ρ_f was estimated from

$$\rho_f = \begin{cases} \dfrac{14{,}670}{d_f} + \rho_w; & d_f > d_s \\ \rho_s; & d_f \le d_s \end{cases} \tag{7}$$

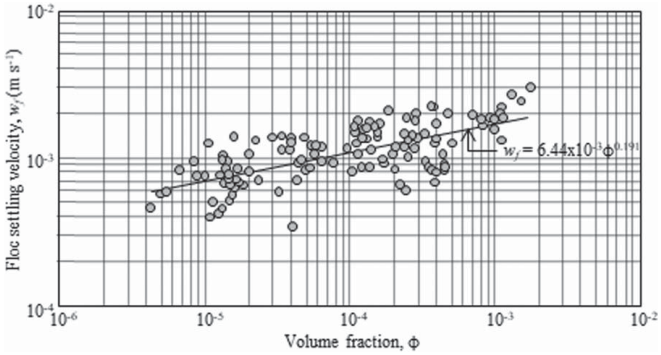

Fig. 5. Variation of Tamar settling velocity with sediment volume fraction and best-fit equation.

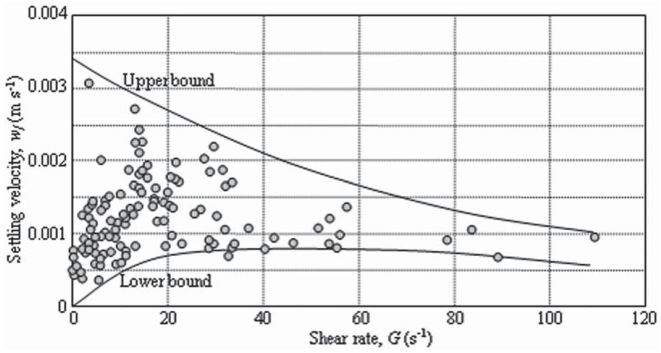

Fig. 6. Variation of Tamar settling velocities with shear rate, and approximate data limits.

From this, the respective floc mass m is given by

$$m = \frac{\pi}{6}\rho_f d_f^3 \tag{8}$$

In Fig. 5, the settling velocity characteristically increases with the sediment volume fraction. This effect is generally attributed to floc growth due to increasing inter-particle collision frequency. The trendline correlation is weak ($R^2 = 0.45$) but visually evident, with a low power-law exponent of 0.19 indicating that the flocs were not highly influenced by sediment concentration. Thus, three orders of magnitude rise in ϕ resulted in only an order of magnitude increase in w_f. The value 0.19 contrasts with some flume observations, such as 1.33 obtained for sediment from San Francisco Bay (Krone 1962), although more typically the values are found to be closer to about 0.33 (Winterwerp and van Kesteren 2004). The low exponent may also reflect the role of organic detritus, which tends to attenuate the influence of electrochemical cohesion. However, as noted later the method of measurement may also have had a role.

Following Manning and Dyer (2002a), a characteristic shear rate G was estimated from

$$G = \sqrt{\frac{\rho_w u_*^3}{\kappa \eta_w z_b}}; \quad u_* = \frac{n\sqrt{g}}{h^{1/6}}u \tag{9}$$

in which u = current velocity nominally at a near-bottom elevation z_b; u_* = bed friction velocity; h = water depth; and κ = von Karman constant (Julien 2010). The elevation of the measurement location, $z_b = 0.03$ mab; and $\kappa = 0.4$ were held constant.

In Fig. 6, all 123 (w_f, G) data points are plotted because the number of measurements per deployment was insufficient to discern trends during a flood or ebb tide. Thus, data spread is in part expectedly due to daily variations in the strengths of flood and ebb, and uncertainties in the measurement of suspended sediment concentration, particularly at low shear velocities. As mentioned in the following, uncertainties may also be related to the characteristics of INSSEV. The settling velocity varies by an order of magnitude at low values of G. With increasing G this range decreases, and as G nears the maximum of 110 s^{-1}, w_f approaches values on the order of 0.001 m s^{-1}. A notable feature of the spread is that in the range of shear rates less than about 16 s^{-1}, there are only two data points with settling velocities exceeding about 0.0015 m s^{-1}, a feature which we will revisit later. In a broader sense, the somewhat notional upper and lower boundaries reasonably define an envelope whose shape is consistent with similar observations from the Gironde, France, and the Dollard at the border between the Netherlands and Germany (Manning and Dyer 2002a). The central question to be addressed is whether the shape of the envelope and the spread within bear a relationship with tide-dependent aggregation.

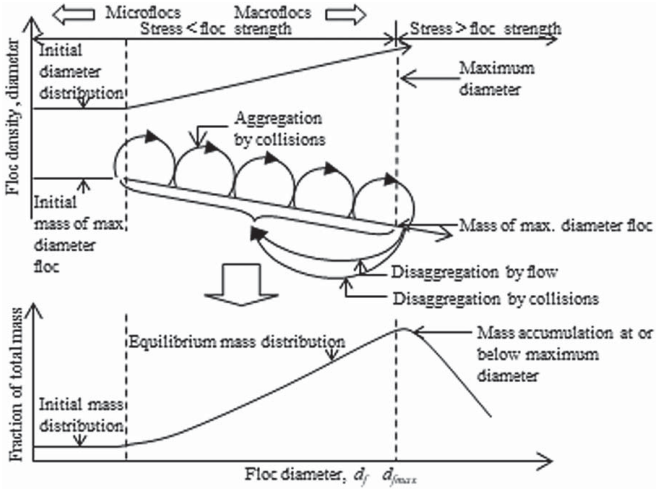

Fig. 7. Schematic of aggregation due to two-body collisions with mass reallocation.

Aggregation Modeling

Steady Flow

Fig. 7 is a schematic diagram of two-body, time-dependent aggregation under assumed conditions of constant flow and total sediment mass. The upper diagram indicates the process by which, beginning with an initial distribution, sediment mass is redistributed with time from small (microflocs, e.g., size <100 μm) to larger (macroflocs >100 μm) size classes by *hops* from left to right until some flocs exceed a maximum diameter $d_{f\max}$. Typically, and concurrently, floc density decreases with increasing size as the flocs acquire increasingly open (less dense) and weak structure. The value of $d_{f\max}$ is that for which the floc shear strength τ_f is equal to or less than the shear stress imposed by interfloc collision or flow shear across a floc. In other words, flocs larger (and weaker) than $d_{f\max}$ break up when they collide or are sheared. The mass of the fragments is subtracted from the larger diameter class and reallocated to smaller classes (by a statistical distribution function), as shown by the two arrow arcs below the bar. After reallocation, the smaller flocs resume hops toward $d_{f\max}$. The lower part of Fig. 7 shows the result of aggregation on mass distribution across size classes.

The initially uniformly distributed mass eventually leads to an equilibrium distribution with a peak at $d_{f\max}$ due to growth pushing floc mass toward that size and breakup moving mass back to smaller diameters.

Fig. 7, which is for illustrative purposes only, oversimplifies aggregation dynamics. For instance, it omits three-body collisions, which produce a different $d_{f\max}$ than two-body collisions; although at the low concentrations encountered in the Tamar, the number of three-body collisions is believed to be a small fraction of the total (McAnally and Mehta 2000). Furthermore, the figure considers a mainly deterministic situation in which it is implied that the flow intensity is constant and floc properties, including strength τ_f, are uniform within each class. The schematic does account for turbulent fluctuations in tidal flow by randomizing the multipliers of flow shear rate and τ_f. The resulting floc mass spectrum is not changed dramatically by randomizing; instead, it becomes somewhat less distinct, with the $d_{f\max}$ line delineating a probabilistic boundary with some flocs larger than $d_{f\max}$, as suggested in the diagram.

Time-Dependent Flow

For simulating aggregation of multiclass particles, the time-dependent mass exchange is numerically calculated for N mass (hence size) classes. Flocs grow or break up under the combined effects of flow shear, differential settling, and Brownian motion as the three canonical collision mechanisms, and mass distribution at each time step is characterized by the size distribution $\varphi(d_f)$. Typically, shear-induced collisions dominate in estuaries and produce the strongest flocs, while differential settling, important close to slack water, generates an order of magnitude weaker flocs (Lick 2009). Thus, as Brownian motion has a minor role in the presence of the other two mechanisms, and differential settling produces weak flocs close to slack water, interest in the present assessment is mainly in the role of shear.

For simulation purposes, each floc class is defined as a mass range with minimum and maximum values of d_f matching the two adjacent upper and lower mass classes, with the midpoint of the range used to calculate a mean diameter and number of flocs in the class. Mean floc settling velocity, excess density, and at given tidal current velocity the shear rate are calculated by Eqs. (5), (6) and (9), respectively. Formulations for deposition and erosion fluxes are not included in the model; instead, decreasing suspended mass with velocity is assumed to result from deposition of the largest flocs, whereas increasing mass due to erosion is accounted for by adding mass to the smallest class.

The floc shear strength τ_f is represented by the fractal relationship from Kranenburg (1994)

$$\tau_f = \delta\left(\frac{\Delta\rho_f}{\rho_w}\right)^{2/(3-D)} = \delta\left(\frac{\Delta\rho_s}{\rho_w}\right)^{2/(3-D)}\left(\frac{d_s}{d_f}\right)^2 \tag{10}$$

where δ = sediment-dependent scaling parameter under the assumption that the shear force (τ_f multiplied by the maximum cross-sectional area of the floc) at floc yield, or breakup point, depends on the density of inter-particle bonds, hence on $\Delta\rho_f$ and D.

From rheometric measurements on several muddy sediments, Krone (1962) reported variable values of τ_f. For instance, in White River, AK the strongest flocs had a shear strength of 4.9 Pa, whereas in San Francisco Bay the value was only 2.2 Pa. Detrital matter may have a significant effect on the scaling parameter δ, such as when a biofilm enwraps clayey mineral agglomerates and increases floc resilience against breakage (Lick 2009). For the San Francisco bay sediment, the shear strength data of Krone (1963) are consistent with $D = 1.9$ and $\delta = 0.75$. On the other hand, when the sediment is mainly organic, depending on the type of organic matter assemblage, the flocs can be weak or strong. For instance, Bache et al. (1999) found that the shear strength of alumino-humic flocs was on average a 100-fold greater than that of San Francisco Bay flocs. Simulations for the Tamar indicated that, with $D = 2$, $\delta = 5$ yielded reasonable values of τ_f.

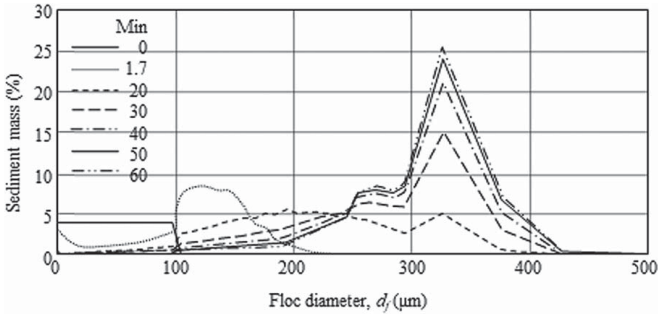

Fig. 8. Illustrative simulation of size spectrum evolution in steady flow.

Floc Growth and Breakup

For simulation purposes, the probability of two-body interfloc collisions was calculated by an extension of the original statistical formulation of von Smoluchowski (1917). Floc collision efficiency α_c, an important determinant of collision probability, is the fraction of collisions that result in either floc growth or breakup (Lick 2009). Difficulty in estimating α_c can be an obstacle to reliable calculations because empirically derived α_c values can vary over four orders of magnitude without a readily discernible correlation with the experimental conditions or sediment properties. Based on the formulation given in McAnally and Mehta (2000), this wide experimental variation was compressed to a range of α_c between 0.1 and 0.7 by a nondimensional expression of floc diameters and density, clay cation exchange capacity (a measure of cohesion), flow velocity and water salinity.

Shear stress τ ($=\tau_{to}$) due to torque from the flow gradient between opposite sides of the floc was computationally imposed across the floc diameter. Stresses τ ($=\tau_{co}$) from collisions were calculated by the conservation of momentum. If τ exceeded a floc's strength τ_f, it was broken into smaller class sizes as a statistical distribution. If colliding flocs were stronger than the imposed stresses, they cohered into a new floc with a mass equal to the sum of the colliding masses. Thus, at each time step, mass could simultaneously move down to smaller size classes by breakup due to τ_{to} or $\tau_{co} > \tau_f$, and up to larger classes by growth from collisions ($\tau_{co} < \tau_f$). Overall, the modeling input parameters were: (1) initial particle density and size; (2) number of floc size classes; (3) initial volume fraction and distribution of sediment mass among size classes; (4) flow shear rate; and (5) salinity.

As an illustration of simulation, Fig. 8 shows the evolution of the size spectrum leading to equilibrium. The physical properties are for the Tamar, but the shear rate is chosen to remain constant at 10 s^{-1}. Calculations are based on the number of floc size classes $N = 52$ and the initial fraction of sediment mass (m) equal to 4% of the total mass in each of the smallest 25 classes. It was found that the initial size distribution became immaterial after about 15 min and did not exert a significant effect on the output. In a manner similar to an experimental demonstration by Lee et al. (2011) using kaolinite flocs settling in a column, starting with the initial floc base diameter of 10.7 μm, aggregation causes a shift in mass from micro to macro sizes, which increase the peak diameter, and at one instant

(20 min) the distribution appears to be distinctly double-peaked. Subsequently, a dominant peak develops at 350 μm, and at 60 min the distribution attains equilibrium configuration. As elaborated upon later, this long duration to reach equilibrium under constant flow conditions may not be achieved under continually varying tidal velocity and shear rate, sediment concentration, and floc mass reallocation. The interpretation of this is that an equilibrium distribution of floc properties does not appear to develop in the Tamar under tidally varying conditions.

Settling in the Tamar

Flow and Floc Transport

Flow and suspended floc transport in the Tamar were characterized by simply considering the study reach to be a uniform open channel with periodic current velocity and constant water density. Thus, we let

$$u = u_0(\sin \sigma t)^{m_0} \tag{11}$$

where u_0 = strength of tidal current devoid of differentiation between flood and ebb; t = time relative to slack water; σ $(=2\pi/T)$ = angular frequency; and m_0 = empirical exponent. Data on September 22 were recorded over one-half tidal cycle from LW slack to HW slack and represented an average condition during the field deployments. In Fig. 9, Eq. (11) is best-fit to the estimated cross-sectional mean current velocity (Manning 2001) on September 22, 1998 over one-half cycle given $\sigma = 0.506$ rad h^{-1} and regression values $u_0 = 1.03$ m s^{-1} and $m_0 = 1.96$. Also shown is the water depth h required to calculate the friction velocity [Eq. (9)].

The relationship between the current, proxied by the friction velocity u_*, and the volume fraction ϕ is shown in Fig. 10 using 390 measurements (including all deployments) bin-averaged over the full range of u_*. The bars, representing ranges of ϕ values with respect to the means (dots), indicate high variability in sediment concentration at low mean velocities, that were likely modulated by comparatively large eddy velocity perturbations. Beginning with no flow, the data suggest a threshold or critical u_* of about 0.006 m s^{-1}, below which the mean volume fraction of 1.6×10^{-5} represents background concentration of detrital matter (Manning 2001).

The u_* value 0.006 m s^{-1} would amount to a critical shear stress of 0.037 Pa, which is smaller than the range 0.17–0.20 Pa deduced independently by Dyer et al. (2002). In any event, the trendline, which for simplicity eschews the existence of the low erosion threshold, indicates an initially rapid, then lower, rate of increase of ϕ with u_*. Although the ϕ values were measured at 0.5 mab, they were generally consistent with depth-mean volume fractions at spring tide between 1.1×10^{-4} and 1.7×10^{-4} reported by Tattersall et al. (2003). This made it feasible to assume that the measured ϕ values were acceptable for the modeled description of the estuary. In Fig. 10, at the highest values of u_* the rate of rise of ϕ is relatively low, suggesting that at high current velocities the supply of fine sediment in this reach of the estuary may be limited by the availability of eroding bed material. Overall, the dependence of ϕ almost solely on u_* makes it convenient to describe aggregation in terms of the shear rate as the primary governing variable.

Simulations and Measurements

In Fig. 11, simulated variations of shear rate G and settling velocity w_f on September 22 are compared with eight measurements on that day. Although in general in both cases the measurements straddle

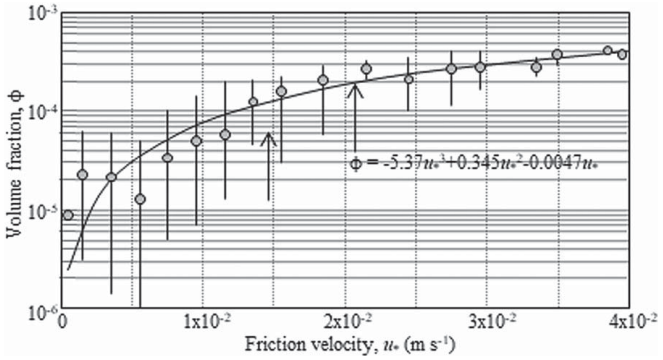

Fig. 9. Tamar current velocity data points and water level curve on September 22, 1998, and Eq. (11) (curve) fitted to the current data.

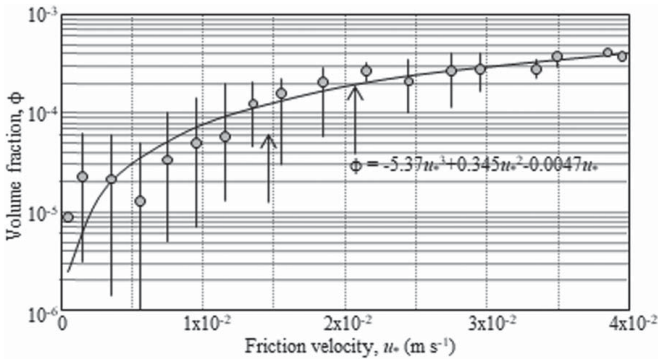

Fig. 10. Variation of suspended sediment volume fraction with bed friction velocity.

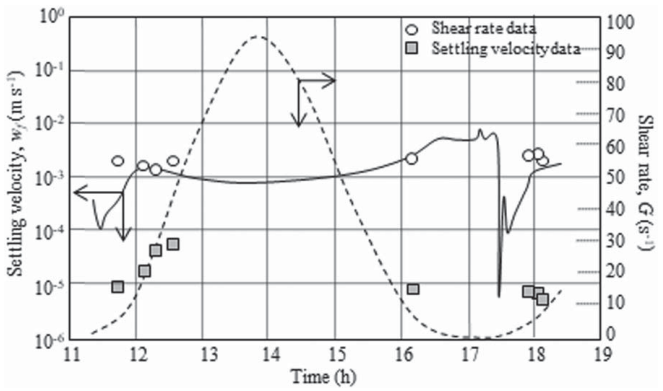

Fig. 11. Comparison of simulated (lines) and observed time series of settling velocities dated September 22.

the respective simulated values, on average the measurements are biased toward higher values compared to the simulations as reflected by RMS errors of 44% and 48% for G and w_f, respectively. A likely reason for bias is believed to be the sensitivity of RMS values to uncertainties in temporal phase shifts, especially during the rapidly rising or falling phases of G and w_f close to LW and HW, respectively. Overall, although the paucity of data precludes fuller validation, there appears to a reasonable match between the measured w_f and its simulated trend of variation except for the notable decline in simulated w_f at about 17.5 hour, which may be the result of differing erosional and depositional algorithms as examined in the following.

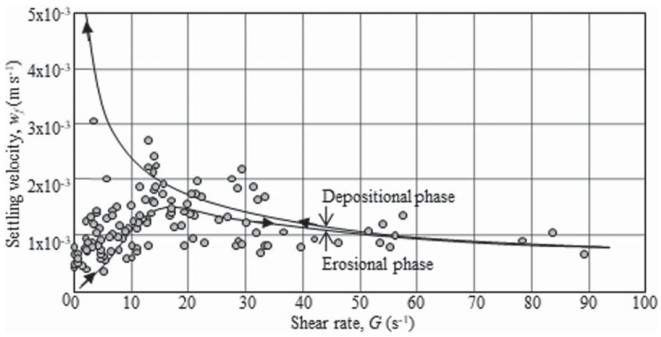

Fig. 12. Simulated (lines) and observed settling velocity variation with shear rate.

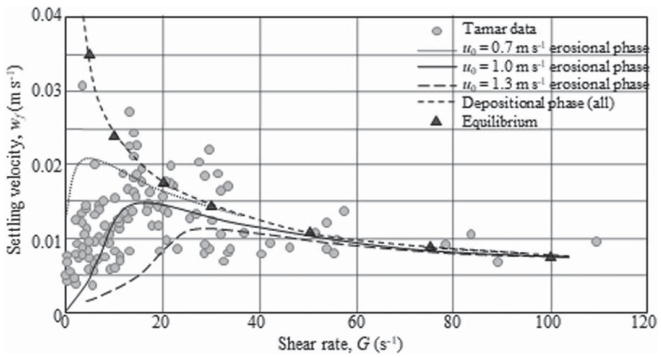

Fig. 13. Settling velocity variation with shear rate: Tamar data and simulations (lines).

In Fig. 12, the observed variation of w_f with shear rate G is compared with simulation, which is differentiated into erosional and depositional phases, i.e., when the shear rate and the volume fraction are rising and falling, respectively. At rates above about 40 s^{-1} the two curves are nearly indistinguishable and match the data. Below 40 s^{-1} the curves divide into two limbs, with the erosional limb reaching a maximum settling velocity at about 15 s^{-1} and then dipping down and following the majority of observed data points that approach a minimum as G approaches the strength of flow. The ensuing depositional curve continues to rise with decreasing G and passes through a cluster of observed values between 10 and 20 s^{-1}. The difference in simulated depositional and erosional phases is caused by an algorithmic difference in how mass is removed from the suspension during deposition and added during erosion, as discussed in the following. Overall, the simulated curves appear to be in reasonable agreement with the data, with the differing depositional and erosional limbs essentially representing the observed data spread. As to the question of what causes the wider variation in observed mean settling velocity at shearing rates smaller than about 15 s^{-1}, simulation of a cycle of smoothly varying shear rate and volume fraction suggests that the observed hysteretic variation of deposition-erosion may be the cause of at least part of the observed spread, with the rest representing tidal variation between spring and neap, as noted further in the following.

Overall, the maximum current velocity u_0 during the deployments ranged between 0.72 and 1.27 m s^{-1} (Manning 2001). Fig. 13 shows the effect of variable u_0; as expected, increasing u_0 from 0.7 to 1.3 m s^{-1} causes a rapid increase in the maximum shear rate at the strength of flow from 33 to 203 s^{-1}, respectively. At the same time, as the tendency of floc breakup increases,

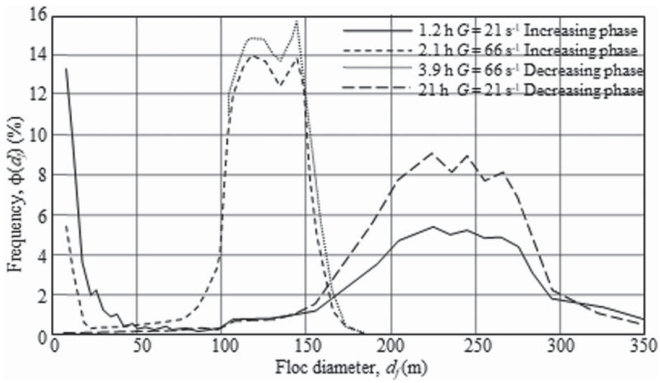

Fig. 14. Simulated size distributions $\varphi(d_f)$ associated with Fig. 13.

Table 2. Parameters of simulated size distributions

Time from slack (h)	G (s^{-1})	Trends of G and φ	φ	d_{fm} (μm)	σ_{dn}
1.2	21	Increasing	1.64×10^{-6}	149	0.93
2.1	66	Increasing	6.00×10^{-6}	109	1.25
3.9	66	Decreasing	7.17×10^{-6}	120	1.02
4.8	21	Decreasing	3.89×10^{-6}	222	0.24

the corresponding peak settling velocity in the erosional phase drops from about 2.2×10^{-3} m s^{-1} at $G = 9$ s^{-1} to about 1.2×10^{-3} m s^{-1} at $G = 23$ s^{-1}. Moreover, settling velocities above $G = 40$ s^{-1} are not significantly influenced by changing u_0, reproducing spread akin to the data. During the depositional phase, changing u_0 does not alter the model relationship between w_f, and G, so the curves lie atop one another. Also shown in Fig. 13 is the variation of equilibrium w_f with G (holding G constant and running the simulation until equilibrium is achieved, as in Fig. 8). In the depositional phase, the equilibrium w_f values are essentially the same as those in the time-varying case. Their magnitudes are partly dependent on the model assumption that the largest, fastest settling flocs deposit first, which downplays the likelihood that at least some of the large and fragile flocs may break and allow smaller flocs to contribute more to the depositing mass. In the erosional phase, the difference between w_f under time-varying tidal current and an equivalent steady current depends on G and the phase of flow, i.e., whether G is less or greater than about 40 s^{-1}, and whether the volume fraction is increasing or decreasing.

Size Spectra

With respect to the relationships between w_f and G in Fig. 13, Fig. 14 shows four simulated size distributions $\varphi(d_f)$ associated with the loci of simulated w_f during the erosional and depositional phases in Fig. 13. These distributions may be subjectively compared with the September 5 measurements in Fig. 2(b). For the erosional phase, during increasing G and ϕ after slack and subsequently decreasing G and ϕ, G values of 21 and 66 s^{-1} (and associated ϕ) have been chosen for illustration. As the tidal current increases during the erosional phase, at 1.2 h after slack water and $G = 21$ s^{-1}, $\varphi(d_f)$ shows two peaks—a sharp peak at small floc sizes and a broad distribution centered at about 240 μm (larger than the mean diameter $d_{fm} = 148$ μm; Table 2) as erosion and shear-induced growth dominate (Fig. 13). At 2.1 h, with $G = 66$ s^{-1} and rising, breakup dominates, and d_{fm} has decreased to 109 μm. During the depositional phase, as G and ϕ decrease, at 3.9 h and 66 s^{-1}, $\varphi(d_f)$ is about the

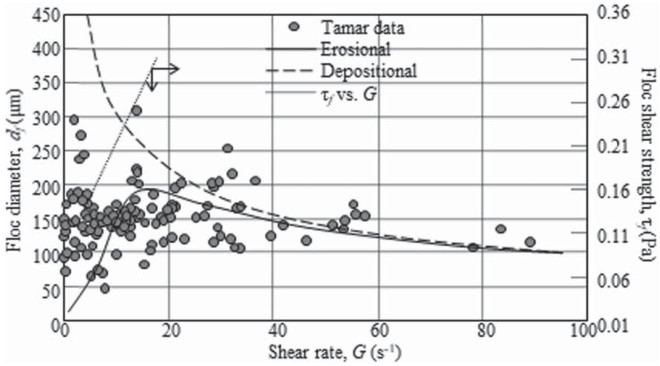

Fig. 15. Measured and simulated (lines) floc diameters and shear strength against shear rate.

same as it was at the same shear rate during the erosional phase. Finally, as the flocs continue to grow, at 4.8 h and $G = 21\ s^{-1}$, large flocs occur with $d_{fm} = 222\ \mu m$.

Unlike the measured distributions with multiple prominent peaks [Fig. 2(b)], the simple simulations display only 2 or 3 small peaks. Tables 1 and 2 indicate that on average the normalized standard deviation σ_{dn} of measured and simulated distributions differ (0.48 and 0.86, respectively). At $G = 21\ s^{-1}$ during the decreasing G phase of deposition, coalescence of flocs produces a nearly uniform distribution with a low value of $\sigma_{dn} = 0.24$.

Method of Measurement

In reference to the preferential breakup of large and weak floc compared to the smaller and stronger ones mentioned previously, it is instructive to ascertain if a bias is present in the measured properties of very weak flocs at low shear rates arising from the procedure required in INNSEV to transfer captured flocs from the upper chamber into the settling column by opening the sliding gate. This assessment is attempted in Fig. 15, which plots measured and simulated diameters for the erosional and depositional phases, as done for w_f in Fig. 12. Also plotted is the floc shear strength τ_f against G calculated from Eq. (10), with d_f values from simulations during the depositional phase. There are two noteworthy observations. One is that the distribution of (d_f, G) points in Fig. 15 differs somewhat from that of (w_f, G) (Figs. 2 and 12). This is so because, as mentioned, the relationship between w_f and d_f [Eq. (2)] includes the floc density ρ_f (Table 1) as the third independent variable.

Another observation is that the τ_f line intersects the curve of decreasing G at about 11 s^{-1}, which is consistent with the paucity of large, measured diameters at low values of G. This suggests a likely, albeit indirect, evidence of the role of the measuring device in causing the breakup of large and weak flocs. Supportive of this effect is that in the range of G less than 14–18 s^{-1}, there is a pile-up of seemingly broken flocs smaller by a factor or two and more than expected during the decreasing G phase.

Concluding Observations

Aggregation modeling indicates that the tidal response of the ensemble of Tamar settling velocities is hysteretic, and generally explains the shape of the data envelope in Fig. 6. Hysteresis occurs because the locus of the settling velocity with shear rate and volume fraction during the second quarter tide (depositional phase) differs markedly from the first (erosional phase), as time shifts in the sediment mass between small and large flocs differ between the two phases. This asymmetry is an important feature of aggregation in tidal flow not captured by analytic formulas.

Further investigation of hysteresis is contingent upon improvement in modeling by explicitly including class-based bed erosion and sediment deposition to describe the change in suspended sediment concentration in a realistic manner. The use of more realistic hydrodynamic modeling accounting for temporal differences in flood and ebb flows as well as spatial variability in the current field coupled with salinity variation can be introduced. For this, synchronous data on flow and sediment are required at multiple points at the estuarine measurement cross section.

Data Availability Statement

Data, models, or code that support the findings of this study are available as follows: The numerical model in McAnally (1999), model simulation results from W.H. McAnally at whmcanally@dsllc.com and unpublished Tamar field observations from A.J. Manning at andymanning@yahoo.com.

Notation

The following symbols are used in this paper:

A = channel cross-sectional area;
C = suspended sediment concentration;
D = fractal dimension;
D_{cal} = calculated fractal dimension;
D_{obs} = observed fractal dimension;
d_f = floc diameter;
d_{fm} = mean floc diameter;
d_{fmax} = maximum diameter;
d_s = base particle (floc) diameter;
f = function of;
G = turbulent flow shear rate;
g = acceleration due to gravity;
h = water depth;
m = particle/floc mass;
m_0 = exponent in Eq. (11);
N = number of d_f classes;
n = Manning's bed resistance coefficient;
P = tidal prism;
Q = mean river discharge;
R^2 = coefficient of determination;
Re_f = floc Reynolds number;
Re* = shear Reynolds number;
T = tidal period;
t = time;
u = current velocity;
u_0 = amplitude of u;
u_* = friction velocity;
w_f = floc settling velocity;
w_{fm} = mean value of w_f;
z_b = near-bed elevation;
α_c = interfloc collision efficiency;
$\Delta\rho_s = \rho_s$ in excess of ρ_w;
$\Delta\rho_f = \rho_f$ in excess of ρ_w;
δ = scaling parameter in Eq. (11);
η_w = dynamic viscosity of water;
κ = von Karman constant;
ρ_f = floc density;
ρ_{fm} = mean floc density;
ρ_s = particle material density;

ρ_w = water density;
σ = tidal frequency;
σ_{dn} = normalized standard deviation of d_f;
σ_{wn} = normalized standard deviation of w_f;
τ = shear stress on the floc;
τ_{co} = stress τ due to interfloc collision;
τ_f = floc shear strength;
τ_{to} = stress τ due to torque on the floc;
ϕ = sediment volume fraction; and
$\varphi()$ = frequency of parameter in brackets

References

Bache, D. H., E. Rasool, D. Moffatt, and F. J. McGilligan. 1999. "On the strength and character of alumino-humic flocs." *Water Sci. Technol.* 40 (9): 81–88. https://doi.org/10.2166/wst.1999.0448.

Christie, M. C., C. P. Quartley, and K. R. Dyer. 1997. "The development of the POST system for in-situ intertidal measurements." In *Proc., 7th Int. Conf. on Electrical Engineering in Oceanography*, 39–45. London: Institution of Electrical Engineers.

Downing, J. P., and R. A. Beach. 1989. "Laboratory apparatus for calibrating optical suspended solids sensors." *Mar. Geol.* 86 (2–3): 243–249. https://doi.org/10.1016/0025-3227(89)90053-4.

Dyer, K. R., A. J. Bale, M. C. Christie, N. Feates, S. Jones, and A. J. Manning. 2002. "The turbidity maximum in a mesotidal estuary, the Tamar estuary, UK: I. Dynamics of suspended sediment." In Vol. 5 of *Fine sediment dynamics in the marine environment—Proceedings in marine science*, edited by J. C. Winterwerp and C. Kranenburg, 203–218. Amsterdam, Netherlands: Elsevier.

Julien, P. Y. 2010. *Erosion and sedimentation*. 2nd ed. Cambridge, UK: Cambridge University Press.

Khelifa, A., and P. S. Hill. 2006. "Models for effective density and settling velocity of flocs." *J. Hydraul. Res.* 44 (3): 390–401. https://doi.org/10.1080/00221686.2006.9521690.

Kranenburg, C. 1994. "The fractal structure of cohesive sediment aggregates." *Estuarine Coastal Shelf Sci.* 39 (5): 451–460. https://doi.org/10.1006/ecss.1994.1075.

Krone, R. B. 1962. *Flume studies of the transport of sediment in estuarial shoaling processes*. Final Rep. Berkeley, CA: Hydraulic Engineering Laboratory and Sanitary Engineering Research Laboratory, Univ. of California.

Krone, R. B. 1963. *A study of rheologic properties of estuarial sediments*. Technical Bulletin 7. Vicksburg, MS: US Army Engineering Research and Development Center.

Lee, B. J., E. Toorman, F. J. Molz, and J. Wang. 2011. "A two-class population balance equation yielding bimodal flocculation of marine or estuarine sediments." *Water Res.* 45 (5): 2131–2145. https://doi.org/10.1016/j.watres.2010.12.028.

Lick, W. 2009. *Sediment and contaminant transport is surface waters*. Boca Raton, FL: CRC Press.

Manning, A. J. 2001. "A study of the effect of turbulence on the settling properties of flocculated mud." Ph.D. thesis, Institute of Marine Studies, Faculty of Science, Univ. of Plymouth.

Manning, A. J., and K. R. Dyer. 2002a. "A comparison of floc properties observed during neap and spring tidal conditions." In Vol. 5 of *Fine sediment dynamics in the marine environment—Proceedings in marine science*, edited by J. C. Winterwerp and C. Kranenburg, 233–250. Amsterdam, Netherlands: Elsevier.

Manning, A. J., and K. R. Dyer. 2002b. "The use of optics for the in situ determination of flocculated mud characteristics." *J. Opt. A: Pure Appl. Opt.* 4 (4): S71–S81. https://doi.org/10.1088/1464-4258/4/4/366.

McAnally, W. H. 1999. "Aggregation and deposition of estuarial fine sediment." Ph.D. thesis, Dept. of Coastal and Oceanographic Engineering, Univ. of Florida.

McAnally, W. H., and A. J. Mehta. 2000. "Aggregation rate of fine sediment." *J. Hydraul. Eng.* 126 (12): 883–892. https://doi.org/10.1061/(ASCE)0733-9429(2000)126:12(883).

McCave, I. N., B. Manighetti, and S. G. Robinson. 1995. "Sortable silt and fine sediment size/composition slicing: Parameters for palaeocurrent speed and palaeoceanography." *Paleoceanography* 10 (3): 593–610. https://doi.org/10.1029/94PA03039.

Migniot, C. 1968. "Étude des propriétés physiques de différents sédiments très fins et de leur comportement sous des actions hydrodynamiques." [In French.] *Houille Blanche* 7: 591–620. https://doi.org/10.1051/lhb/1968041.

Strom, K., and A. Keyvani. 2011. "An explicit full-range settling velocity equation for mud flocs." *J. Sediment. Res.* 81 (12): 921–934. https://doi.org/10.2110/jsr.2011.62.

Tattersall, G. R., A. J. Elliot, and N. M. Lynn. 2003. "Suspended sediment concentrations in the Tamar estuary." *Estuarine Coastal Shelf Sci.* 57 (4): 679–688. https://doi.org/10.1016/S0272-7714(02)00408-0.

Teeter, A. M., 2001. "Clay-silt sediment modeling using multiple grain classes. Part I: Settling and deposition." In *Coastal and estuarine fine sediment processes*, edited by W. H. McAnally and A. J. Mehta, 157–171. Amsterdam, The Netherlands: Elsevier.

Uncles, R. J., et al. 2003. "Intertidal mudflat properties, currents and sediment erosion in the partially mixed Tamar Estuary, UK." *Ocean Dyn.* 53 (3): 239–251. https://doi.org/10.1007/s10236-003-0047-6.

van Leussen, W. 1994. "Estuarine macroflocs and their role in fine-grained sediment transport." Ph.D. thesis, Faculty of Geosciences, Univ. of Utrecht.

von Smoluchowski, M. Z. 1917. "Versuch einer mathematischen theorie der koagulationskinetic kolloider losungen." *Z. Phys. Chem.* 92: 129–168.

Winterwerp, J. C., and W. G. M. van Kesteren. 2004. *Introduction to the physics of cohesive sediment in the marine environment*. Amsterdam, Netherlands: Elsevier.